HHS Public Access

Author manuscript

ACS Appl Mater Interfaces. Author manuscript; available in PMC 2020 January 18.

Published in final edited form as:

ACS Appl Mater Interfaces. 2019 September 18; 11(37): 33548–33558. doi:10.1021/acsami.9b08341.

Electrospun Fiber Mesh for High-Resolution Measurements of Oxygen Tension in Cranial Bone Defect Repair

Kevin Schilling[†,‡], **Mirna El Khatib**[§], **Shane Plunkett**[§], **Jiajia Xue**[¶], **Younan Xia**[¶], **Sergei A. Vinogradov**[§,*], **Edward Brown**[†,*], **Xinping Zhang**[†,‡,*]

[†]Department of Biomedical Engineering, University of Rochester, Rochester, NY 14620, USA

[‡]Center for Musculoskeletal Research, University of Rochester, School of Medicine and Dentistry, Rochester, NY 146421, USA

[§]Departments of Biochemistry and Biophysics and of Chemistry, University of Pennsylvania, Philadelphia, PA 19104, USA

[¶]The Wallace H. Coulter Department of Biomedical Engineering, Georgia Institute of Technology and Emory University, Atlanta, GA 30332, USA

Abstract

Tissue oxygenation is one of the key determining factors in bone repair and bone tissue engineering. Adequate tissue oxygenation is essential for survival and differentiation of the bone-forming cells and ultimately the success of bone tissue regeneration. Two-photon phosphorescence lifetime microscopy (2PLM) has been successfully applied in the past to image oxygen distributions in tissue with high spatial resolution. However, delivery of phosphorescent probes into avascular compartments, such as those formed during early bone defect healing, poses significant problems. Here we report a multifunctional oxygen-reporting fibrous matrix fabricated through encapsulation of a hydrophilic oxygen-sensitive, two-photon excitable phosphorescent probe PtP-C343 in the core of fibers during coaxial electrospinning. The oxygen-sensitive fibers support bone marrow stromal cell (BMSC) growth and differentiation, while at the same time enable real-time high-resolution probing of partial pressures of oxygen (pO_2) via 2PLM. The hydrophilicity of the probe further facilitates its gradual release into the nearby microenvironment, allowing fibers to act as a vehicle for probe delivery into the healing tissue. In conjunction with a cranial defect window chamber model, which permits simultaneous imaging of the bone and neovasculature *in vivo* via two-photon laser scanning microscopy (2PLSM), the oxygen reporting fibers provide a useful tool for minimally invasive, high-resolution, real-time 3D mapping of tissue oxygenation during bone defect healing, facilitating studies aimed at understanding the healing process and advancing design of tissue engineered constructs for enhanced bone repair and regeneration.

[*]**Corresponding authors contact information:** Xinping Zhang, The Center for Musculoskeletal Research, University of Rochester Medical Center, 601 Elmwood Avenue, Rochester, NY 14642, USA, Xinping_Zhang@urmc.rochester.edu; Edward Brown, Department of Biomedical Engineering, University of Rochester, Goergen Hall Box 270168Rochester, NY 14642, USA, Edward_brown@urmc.rochester.edu; Sergei A. Vinogradov, Department of Biochemistry and Biophysics, Perelman School of Medicine, Department of Chemistry, School of Arts and Sciences University of Pennsylvania Philadelphia, PA 19104, vinograd.upenn@gmail.com.

Supporting Information. Outer fiber diameter distribution from SEM images. Schematic of 2PLSM System. Calibration of PtP-C343 inside fibers. PtP-C343 in-fiber calibration at varying probe concentrations. Longitudinal oxygen reporting fibers within cranial defect.

Graphical Abstract

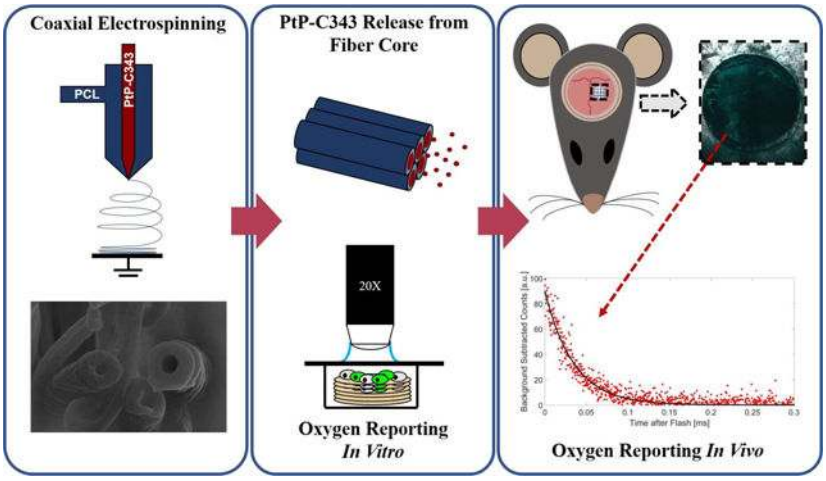

Keywords

bone repair; coaxial electrospinning; oxygen tension; phosphorescence quenching; 2-photon laser scanning microscopy; two-photon phosphorescence lifetime microscopy

1. INTRODUCTION

Bone tissue repair and regeneration is a complex process that requires spatial and temporal coordination of multiple cellular compartments in concert with integrated signaling pathways. This process is further influenced by a myriad of microenvironmental factors that impact the cellular and molecular events that take place during repair and regeneration.[1–4] One of the key microenvironmental factors that plays a pivotal role in the complex bone repair process is oxygenation of the bone-forming tissue. Given the fact that oxygen diffusion distances in tissue are limited to 100–200 μm from the nearest capillary, adequate distribution and sufficient supply of oxygen is essential to support cell growth and to guide uniform bone formation.[5–6] It has been shown that the state of low oxygenation, known as hypoxia, plays an important role in the regulation of osteogenesis and angiogenesis in bone development and repair.[7–8] Genetic manipulation of the central player in cellular response to hypoxia, known as hypoxia inducible factor 1α (HIF-1α), leads to profound changes in the skeletal system.[9–12] However, how hypoxic microenvironment initiates and directs osteogenesis and angiogenesis remains poorly understood. On one hand, hypoxia is critical for the initiation of repair and revascularization of the engineered tissue. On the other hand, persistent hypoxia can lead to extensive fibrotic tissue formation, which impairs progression of progenitor cell differentiation and bone formation.[13–14] It remains unknown how local oxygen tension affects vessel formation and remodeling, and thereby controls switching between bone and fibrotic tissue formation. Establishing the ability to quantify bone tissue oxygenation *in vivo* will advance our understanding of the healing mechanisms and ultimately help to devise more effective strategies to improve bone repair and reconstruction.

The oxygen levels in a biological tissue can be measured by the phosphorescence quenching method using probes with controllable quenching parameters and defined bio-distributions.[15–17] The method is based on the ability of molecular oxygen to efficiently quench emission from excited triplet state of probe molecules. Tissue oxygen levels are derived from measurements of the triplet decay times, which are independent of the local probe concentrations and/or optical properties (*e.g.*, absorption and scattering heterogeneities) of the medium. Numerous oxygen sensing materials have been developed over the years and applied to various biological systems.[18–22] Among the existing phosphorescent chromophores, complexes of platinum (Pt) and palladium (Pd) porphyrins are the best available choice for *in vivo* tissue-level imaging applications due to their strong visible-to-near-infrared absorption bands and microsecond-scale phosphorescence decay times. When encapsulated inside dendrimers with hydrophilic periphery, Pt and Pd porphyrins make up a family of 'protected' oxygen probes,[23–24] which permit truly quantitative and selective measurements of oxygen in biological environments.

An imaging technique that combines phosphorescence quenching with two-photon laser scanning microscopy (2PLSM) has recently been developed.[25] This approach, known as two-photon phosphorescence lifetime microscopy (2PLM), capitalizes on well-known advantages of two-photon excitation for tissue-level imaging,[26] enabling oxygen measurements in 3D with high spatial resolution. To date, 2PLM has been successfully applied in neuroimaging,[27–34] stem cell biology[35–37] and more recently in cancer immunology.[38] In bone tissue, two-photon microscopy provides additional advantage for imaging newly formed bone *via* second harmonic generation (SHG).[35, 39] In view of the important role of oxygen in cellular metabolism, tissue specification as well as neovascularization, establishing a tool that allows simultaneous analyses of oxygen distributions and bone regeneration via two-photon microscopy would greatly benefit studies that focus on progenitor cell interactions with bone healing microenvironment.

In order to perform oxygen imaging by 2PLM, phosphorescent probes,[25, 40–42] such as PtP-C343, have to be delivered into the tissue, either *via* injection into the blood or directly into the interstitial space for extravascular oxygen measurements.[27–28] In tissues with leaky vasculature probes can accumulate in the interstitial space over time due to their leakage from the blood vessels.[35] However, in tissues that have not yet been vascularized and/or cannot be disturbed during the critical early phase of healing, probe delivery poses a major problem.

Electrospun fibers have been increasingly recognized as a biomimetic platform for bone tissue engineering due to their versatility in mimicking extracellular matrix (ECM)[43–46] as well as for the benefits of their high surface-to-volume ratios for cell attachment, drug loading and mass transport.[47–48] In particular, coaxially electrospun nanofibers have recently emerged as promising matrices for controlled release of hydrophilic drugs for therapeutic purposes.[49–50] Phosphorescent oxygen-sensitive dyes have previously been incorporated into electrospun fibers[20, 51–55] as well as other polymeric materials for oxygen sensing.[36, 56–57] However, so far only a few of these materials have been used in combination with two-photon excitation.[58–59] Furthermore, in all reported systems, the oxygen sensitive molecules were either covalently bound to the supporting matrix or remained a part of the polymer

material due to the high hydrophobicity of the molecules. As a result, oxygen sensing could be performed only within the fibers themselves (or other solid-state matrix), while the surrounding medium remained probe-free.

With the goal of developing a multifunctional tissue scaffold, capable of supporting progenitor cell growth and differentiation, while allowing measurements of oxygen tension in the healing tissue, we employed a different probe encapsulation strategy. A highly hydrophilic two-photon-excitable phosphorescent probe PtP-C343,[2325] was incorporated into an electrospun fiber mesh *via* coaxial electrospinning. Due to its hydrophilicity, PtP-C343 has propensity to leach out from the matrix into the surrounding tissue, where it can function independently as a soluble oxygen sensor. We show that by controlling the conditions of the fiber preparation, the PtP-C343-encapsulating fiber mesh can be optimized for quantitative pO_2 measurements throughout the healing tissue at the early stages of tissue repair, when intravascular or direct interstitial delivery of the probe into the bone is not yet possible. The new multifunctional biomimetic oxygen-sensing matrix, capable of oxygen probe delivery into the tissue, should assist studies aimed at elucidation of the role of oxygen and hypoxia in bone tissue engineering-mediated repair and reconstruction.

2. MATERIALS AND METHODS

2.1. Materials.

Polycaprolactone (PCL) [*Mw*=80 kDa] and polyethylene glycol (PEG) [*Mw*=35 kDa] were purchased from Sigma Aldrich (St. Louis, MO, USA). Hexafluoro-2-propanol (HFIP) was purchased from Oakwood Chemical (Estill, SC, USA). Two-photon oxygen probe PtP-C343 was synthesized as previously described.[25, 60]

2.2. Experimental Animals.

B6.Cg-Gt(ROSA)26Sor$^{tm9(CAG-tdTomato)}$ reporter mice, also known as Ai9 mice, were originally purchased from Jackson Laboratory (Bar Harbor, ME). Endothelial cells specific Cdh5-CreER^{T2} mice were obtained from Dr. Ralf Adams through Material Transfer Agreement. All *in vivo* experiments were performed using adult mice of 8–12 weeks old housed in pathogen-free, temperature and humidity-controlled facilities with a 12h day-night cycle in the vivarium at the University of Rochester Medical Center. All cages contained wood shavings, bedding and a cardboard tube for environmental enrichment. All experimental procedures were reviewed and approved by the University Committee on Animal Resources. General anesthesia and analgesia procedures were performed based on the mouse formulary provided by the University Committee on Animal Resources. The health status of the animals was monitored throughout the experiments by experienced veterinarians according to the Guide for the Care and Use of Laboratory Animals outlined by the National Institute of Health.

2.3. Coaxial Electrospinning.

Coaxial fibers were electrospun by pumping two separate sheath and core solutions into a custom-made coaxial needle. The sheath solution comprised of 12% w/v PCL dissolved in HFIP. To build a base for the core solution, a 10% polyethylene glycol (PEG) (35 kDa)

solution in DI-water was used. PtP-C343 was added to the PEG mixture to reach the final concentration of 50 μM. Concentration of PtP-C343 was optimized based on results from the release experiments. All mixtures were prepared at room temperature and stirred until homogeneous solutions were obtained. A voltage (10 kV) was applied between the steel coaxial needle and a grounded copper sheet (collector) separated by 11 cm distance from the tip of the needle. Fibers spun from the needle were collected onto a sterilized filter paper (Munktell Filtrak, Grade 1F, Fisher Scientific) placed on the top of the copper sheet. The electrospinning process was carried out at room temperature at the environmental relative humidity of 40%. Coaxial fibers were separately spun at four combinations of sheath/core flow rates: 2.0/0.2, 2.0/0.4, 4.0/0.2, and 4.0/0.4 mL/h.

2.4. Characterization of Coaxial Fibers.

Coaxial electrospun fibers were sputter-coated with gold nanoparticles and imaged under a scanning electron microscope (ZEISS Sigma 300, URNano). To observe the cross-section of the coaxial fibers, fiber meshes were freeze-fractured in liquid nitrogen and placed on a sample stub with the broken ends perpendicular to the stub. Scanning electron microscopy (SEM) was used to evaluate the fiber morphology, diameters, and fiber size distribution. Additionally, coaxial fibers spun at each flow rate combination were placed onto copper mesh discs and imaged *via* transmission electron microscopy (TEM) to examine the presence of hollow structures.

The surface wettability of PtP-C343-encapsulating fiber meshes was determined by the sessile drop method.[61] A water droplet (10μL) was placed onto the fibers and immediately imaged *via* a camera. Images were processed, and the contact angle of the droplet was determined using the DropSnake plugin created in Fiji.[62] Young's modulus and tensile strength of the fiber meshes were measured in a mechanical testing instrument (Instron 8841, Norwood, MA). Fiber meshes were stretched at a rate of 60 mm/min until failure.

2.5. PtP-C343 Release from Coaxial Fibers.

Fiber meshes containing PtP-C343 were weighed and placed in the wells of a 24-well plate containing phosphate buffered saline (PBS) (1 mL per well). Fibers were incubated at 37°C for the duration of the experiment. At designated time intervals, PBS solutions containing released PtP-C343 were transferred into the wells of a 48-well plate. The luminescence of the solutions was analyzed using a microplate reader (Synergy Mx, Biotek, Winooski, VT) along with blank and standard solutions containing known concentrations of PtP-C343 (molar extinction coefficient, ε=26,000 $M^{-1}cm^{-1}$ at λ_{max}=517 nm). The fluorescence intensity of each well was quantified at the wavelengths corresponding to the fluorescence excitation and emission for PtP-C343 (400 nm and 498 nm, respectively). Fluorescence intensity of the released PtP-C343 (2,000–25,000 counts) was higher than background (500 counts) at each time point when measuring the release. Using the standard curve, the amounts of the released PtP-C343 were calculated at each time interval. At the end of the release period, the fiber meshes were dissolved in 1 mL of HFIP: DI-water solution (1:1 vol.), and the amount of remaining PtP-C343 in the fiber meshes was calculated from the fluorescence intensity of the solutions. The accumulated release was calculated by dividing

the amount of the probe in solution at each time interval against the sum of the total released amount and the remaining amount of probe in the fiber at the end point of the experiments.

2.6. Fiber Payload Determination.

The payload of PtP-C343 within the fibers was determined by completely dissolving the electrospun fiber meshes of known weight in a mixture of HFIP and DI-water (1:1 vol.), followed by measuring the fluorescence intensity of the solution using a fluorescence microplate reader. The amount of loaded PtP-C343 from each type of fiber mesh was calculated based on the fluorescence intensity and the linear standard curve of PtP-C343. The payload per mg of fiber mesh was calculated and plotted.

2.7. Two-photon Laser Scanning Microscopy (2PLSM).

A two-photon microscope with a tunable Mai Tai laser (100 fs, 80 MHz; Spectra-physics, Santa Clara, CA) for excitation and a modified Olympus Fluoview 300 confocal unit was used for imaging. The scheme of the imaging setup is shown in Figure S2. An Olympus water immersion objective lens LUMPlan fI/IR 20X/0.95NA and a C-Apochromat 10X/0.45 (Zeiss) were used to image bone *in vivo via* Second Harmonic Generation (SHG) and blood vessels *via* tdTomato Red fluorescence (RFP) of labeled endothelial cells in Cdh5-CreER^{T2}; Ai9 mice. Images (1024×1024 pixels) were acquired at a rate corresponding to the pixel dwell time of 0.2 ms with the laser tuned to 810nm for SHG and 900nm for RFP, respectively. The autofluorescence of PCL fibers, fluorescence of RFP and SHG were collected with a 534/30 nm, a 605/55 nm and a 405/30 nm bandpass filters (Semrock), respectively.

2.8. Instrument Settings for Phosphorescence Lifetime Measurements and pO_2 Determination.

Excitation of PtP-C343 was performed at 900 nm. The light transmitted through the dichroic was passed through a 706/167 nm band-pass filters and directed onto a PMT (Hamamatsu R10699, Shizuoka, Japan) for quantification of PtP-C343 phosphorescence (λ_{max} 680 nm). A Pockels cell, which was used to modulate the train of high repetition rate pulses, generated 10 μs-long excitation gates every 1.3 ms to excite PtP-C343. The time-averaged power at the sample during the excitation gate (when the Pockels cell was fully transmitting light), was set to 80 mW for *in vitro* experiments and 160 mW for *in vivo* experiments. PtP-C343 phosphorescence was detected by a photon counting PMT and a photon counting system (SR 400, Stanford Research Systems, Sunnyvale, CA). The counts were binned into 320 ns-long bins. Typically, 2000 excitation-collection cycles were averaged to achieve adequate signal-to-noise ratios (SNR>1.5). Data acquisition was controlled using software custom-written in LabView (National Instruments).

Raw phosphorescence decay data were fit to a single exponential function after subtraction of the offset, to determine the decay time constant, τ (Eq. 2):

$$I(t) = A \times e^{\frac{-t}{\tau}},$$

where I is the emission intensity (after subtraction of the offset), A is the amplitude, and τ is the decay time constant. Using an independently measured calibration curve, τ was converted into oxygen tension (pO_2). Due to the reciprocal relationship between the phosphorescence signal and oxygen concentration, the accuracy of the measurement increases as oxygen concentration drops. Therefore, at low oxygen levels accuracies of $\Delta pO_2 < 0.1$ mmHg are easily achievable provided sufficiently long data acquisition periods (e.g. several seconds).

2.9. Calibration of PtP-C343 Inside Coaxial Electrospun Fibers.

PtP-C343 in solution was calibrated as described previously.[24–25] The setup used for calibrations of the probe inside the fibers is shown in Figure S3A. A glass vial (ca. 2 cm in diameter) with a gas-impermeable stopper and magnetic stirring bar was positioned inside a thermostat, equipped with a magnetic stirrer. Temperature inside the chamber was controlled with ± 0.1°C accuracy. A solution of PtP-C343 (ca. 2 mL, 5 μM) was added to the vial. A piece of the fiber mesh was attached to the wall of the vial (by surface adhesion) above a porous disk, which was placed in the vial to prevent sliding of the mesh into the solution if it were to fall off the wall. Two pairs of optical fibers (3 mm in diameter) for excitation and collection of phosphorescence were used: one pair against the mesh and the other against the solution. The fibers were connected to the optical ports of two LED-based time-domain phosphorometers, as described previously.[24] The optical fibers in the phosphorometers were selected to match the excitation and emission bands of PtP-C343. The phosphorescence was excited by 5 μs-long LED pulses and registered during 1 ms by an avalanche photodiode (Hamamatsu C12703–01), whose output was digitized at 500 kHz (NI 6341 USB, National Instruments). Typically, 200 excitation cycles were averaged to obtain a phosphorescence decay. The vial was closed with a stopper containing two gas ports for argon and left to equilibrate at a desired temperature (22°C or 36.6°C), while the phosphorescence from both the mesh and the solution was continuously measured in 10 s intervals. Complete equilibration of the solution typically took about 5 min, while equilibration of the mesh required up to 20 h (Figure S3B), presumably due to its slow hydration. It is important to mention that the mesh was kept fully hydrated during the entire calibration procedure, because the gas phase in the vial was saturated with water vapor.

2.10. Bone Marrow Stromal Cell Isolation and Culture.

Bone marrow stromal cells (BMSCs) were isolated from 8–12 weeks-old global GFP transgenic mice as previously described.[63–64] Briefly, bone marrow was flushed from the marrow cavity by slowly injecting α-MEM at one end of the bone using a sterile 21-gauge needle. The marrow suspension was dispersed gently by pipetting several times to obtain a single cell suspension. The cell suspension was further filtered through a 70 μm cell strainer (Falcon) to remove debris. About 5×10^6 isolated bone marrow stromal cells were seeded on each sterile PtP-C343-containing electrospun fibrous mesh (fabricated from the condition of 4.0/0.4 mL/h flow rate) in 12-well plates and cultured in α-MEM media containing 15% fetal bovine serum (Sigma-Aldrich, St. Louis, MO) for 10 days. Osteogenic differentiation media containing 50 μg/mL ascorbic acid (Sigma-Aldrich, St. Louis, MO), 5 mM β-glycerophosphate (Sigma-Aldrich, St. Louis, MO), and 10% FBS in α-MEM was added at day 7 with media change every two days.

2.11. Evaluation of BMSC Attachment, Growth and Differentiation on Coaxial Fibers.

Fiber meshes seeded with GFP^+ BMSCs were imaged via an inverted epifluorescence microscope at days 5, 7, 10, and 15 to determine cell attachment and growth on the fibers with or without PtP-C343. To determine the osteoblastic differentiation of the cultured BMSCs on the scaffolds, alkaline phosphatase (ALP) staining was performed on day 15 following seeding. For ALP staining, cells were fixed in ethanol, followed by staining with substrates containing 0.2 mg/mL naphthol AS-MX phosphate and 0.4 mg/ml Fast red TR in buffer (100 mM Tris-HCl, pH 8.3, 100 mM NaCl, 10 mM $MgCl_2$). Stained fiber meshes were photographed by a digital camera mounted on a microscope (Olympus SZX12). The numbers of ALP^+ colonies on the fiber mesh were recorded and manually counted. The areas of the ALP^+ region were quantified using Image J.

2.12. In vitro Measurements of pO_2 Using PtP-C343-containing Coaxial Fibers.

The fiber meshes with or without PtP-C343 were removed from 12-well plate at days 7, 10, and 15 following BMSC-seeding, and placed into a cassette with a glass top for cell/fiber visualization and pO_2 reporting. The cassettes were placed in a cell incubator (37°C, 95% air, 5% CO_2) for 30 minutes prior to imaging. Oxygen tension was calculated using the decay time constant (τ) and the calibration curve as described above. PtP-C343 (10μM) was added into the culture media to obtain pO_2 readings in the experiments with non-PtP-C343 containing fibers. The pO_2 readings from PtP-C343 containing fibers and from PtP-C343 in solution were recorded separately. Arbitrary point measurements were made in the fibers or in media within the cassette regardless of GFP cell location.

2.13. Real-time pO_2 Measurements in Cranial Defect Window Chamber Model.

To determine the oxygen reporting capability of the PtP-C343-containing fiber mesh in defect repair, a cranial defect window chamber model was created in mice as previously described.[39] Briefly, a 2-mm full thickness defect was created in the parietal bone of the calvarium in C57BL/6J mice using a 1.8 mm size Busch inverted cone bur (Armstrong Tool & Supply Company, Livonia, MI). Using a biopsy punch, a sterilized circular graft of 2 mm in diameter containing 10 layers of stacked fiber meshes spun at 4.0/0.4 mL/h flow rate was cut and transplanted into the cranial defect of the same size. A glass window was mounted on top of the wound for imaging. Wide-field imaging *via* a stereo microscope (Olympus, Waltham, MA) was used to monitor vessel formation during cranial bone defect healing, followed by 2PLSM and 2PLM at 3, 7, 11, 19, and 32 days post-surgery. Using point scans, pO_2 measurements were made in target areas within the defect and surrounding tissues. Three different zones within the defect with varying distances to the edge of the bone were selected for 2PLM scanning. At least 9 measurements were made randomly within each zone by point scans.

To measure pO_2 in interstitium and vessels, Cdh5-$CreER^{T2}$; Ai9 mice were treated with a 10 mg/mL dose of Tamoxifen in corn oil via intraperitoneal injection every 2 days for 3 times to induce vascular endothelial cell production of a red fluorescent protein. Upon completion of Tamoxifen dosage, the cranial window defect chamber model was established with oxygen reporting fibers inserted into the defect as described above. 2PLSM and 2PLM were conducted to obtain pO_2 around vessels where fibers were located at 11-day post-surgery.

Measurements of pO_2 within vessels were obtained following retro-orbital injection of 15 μM PtP-C343 within the cranial defect. Point scans were centered on target vessels and the nearby interstitial spaces where fibers were located. A mean of at least 3 measurements made on each location was used to compare pO_2 values in and around vessels.

2.14. Statistical Analyses.

SEM measurements, release data, and pO_2 reports are expressed as mean ± standard error. Statistical analyses were conducted using a one or two-way Analysis of Variance (ANOVA) with Bonferroni post-tests to compare groups unless otherwise specified. A p value less than 0.05 was considered statistically significant.

3. RESULTS AND DISCUSSION

3.1. Fabrication and Characterization of Coaxial Fibers.

As an FDA-approved, inexpensive, biocompatible and biodegradable polymer PCL has been successfully used in various bone tissue engineering applications.[64–67] The PCL polymer undergoes hydrolytic degradation due to the presence of hydrolytically labile aliphatic ester linkages, with reported rate of degradation of 2–3 years.[68] PCL has been used previously for encapsulation of luminescent dyes for oxygen sensing.[55] PEG is a biologically inert, non-immunogenic, and water-soluble polymer that is immiscible with PCL. PEG has previously been used with PCL to create core sheath electrospun fibers for controlled delivery of hydrophilic molecules.[69–71] PEG increases the viscosity of the solution thus enables the consistent production of core/sheath electrospun fibers production, as well as stabilization of the core components.[72–74]

To obtain coaxial fiber meshes, PEG and PCL solutions of varying concentrations were used to produce the electrospun fibers with a core-sheath structure. Based on the results obtained by SEM, 10% PEG (w/v, core) and 12% PCL (w/v, sheath) were the optimal concentrations for generating coaxial fibers with desired uniformity and reproducibility. To examine the impact of the inner “core” and outer “sheath” flow rates on the inner and outer diameters of the core/sheath fibers, combinations of flow rates 2.0/0.2, 2.0/0.4, 4.0/0.2, and 4.0/0.4 mL/h (sheath/core flow rates, respectively) were tested for the coaxial electrospinning. Analyses using SEM and TEM showed that all four combinations of the flow rates produced bead-free fibers with a hollow structure (Figure 1, A–C and Figure S1). The average outer diameters corresponding to the flow rates of 2.0/0.2, 2.0/0.4, 4.0/0.2, and 4.0/0.4 were 0.75 ± 0.33, 1.10 ± 0.51, 0.79 ± 0.28, and 0.70 ± 0.30 μm, respectively. The combination of the flow rates 4.0/0.2 yielded a greater outer diameter than the other three groups (Figure 1D). The 0.4 mL/h core flow rate produced fibers that had a greater inner/outer diameter ratio than those of 0.2 mL/h core flow rate (Figure 1E) ($p<0.05$ One-way ANOVA, Bonferroni Post-test).

3.2. PtP-C343 Encapsulation and Release:

PtP-C343, a hydrophilic phosphorescent probe, was encapsulated within the PEG core of the fibers through coaxial electrospinning. PtP-C343 with its own external PEG layer ensures uniform probe distribution within the fibers. The release of PtP-C343 from the fibers was examined over 20 days. Similar release rates were observed in all four samples prepared

using different combinations of flow rates (Figure 2A, $p>0.05$). A gradual but continuous release of PtP-C343 was observed over a period of 20 days with about 50% probe remained in the fibers at the end point of the experiments. Further analysis of the amount of payload showed that the fibers prepared at a core flow rate of 0.4 mL/h contained more PtP-C343 than those prepared at a core flow rate of 0.2 mL/h (Figure 2B, $p<0.05$). The 2.0/0.4 mL/h group had the highest content of payload, which was consistent with the diameter ratio measurements (Figure 1E). Negative control fibers that contained only PEG within the core, showed no fluorescence in either release or payload experiments.

Additional characterization of core sheath fibers revealed that PtP-C343-encapsulating fibers had a mean Young's Modulus of 4.70 ± 0.62 MPa and a tensile strength of 0.56 ± 0.04 MPa (n=6 fiber mesh strips). Wettability studies demonstrated that these fibers had a mean contact angle of 121 ± 2.7° (n=4 fiber meshes), consistent with those previously described in literature.[61, 75–76]

3.3. Calibration of PtP-C343-containing Coaxial Fibers.

When PtP-C343 is encapsulated inside a polymer PCL sheath, the efficiency of the phosphorescence quenching by oxygen might be altered compared to that in solution. To avoid ambiguity in pO_2 measurements, the probe was calibrated directly in the fibers (Figure S3). Calibrations were performed for multiple meshes (n=5) (Figure S3C) and in fibers containing 10 μM, 20 μM and 50 μM of PtP-C343 (Figure S4). Since PtP-C343 in solution was calibrated independently, readings from the solution provided reference pO_2 values, against which the phosphorescence lifetimes of the probe in the mesh were plotted and fitted to an arbitrary function. As shown in Figure 3, the calibration plots for PtP-C343 encapsulated in PCL fibers and for PtP-C343 in solution were quite close, deviating only at higher pO_2 values. Furthermore, the calibration plots of PtP-C343 within the fibers were practically invariant of its concentration in the range of up to 50 μm of PtP-C343, suggesting that oxygen quenching of the phosphorescence within the fibers is independent of the probe concentration (Figure S4). For the purpose of this study we used the PtP-C343-in-fiber calibration curve for pO_2 measurements when the excitation beam was focused on a fiber, and the calibration curve for the probe in solution for pO_2 measurements when the phosphorescence was excited e.g. in solution or blood vessels.

3.4. PtP-C343-containing Fibers Support Skeletal Progenitor Cell Growth and Differentiation in Culture While Retaining Oxygen Reporting Capability.

To determine whether PtP-C343-containing fibers have a negative impact on bone forming progenitor cells, BMSCs were isolated from GFP transgenic mice and cultured for 2 weeks on the coaxial PtP-C343-containing fibers and the control PEG-containing core-sheath fibers. As shown in Figure 4A, PtP-C343-containing fibers had no discernable effects on the attachment, growth, or differentiation of BMSCs as compared to the controls. BMSCs were readily differentiated into ALP^+ osteoblastic colonies following osteogenic induction (Figure 4B). No difference was observed in number or size of the ALP^+ colonies between PtP-C343 containing and control PEG fibers at day 15 (Figure 4C and D).

To determine the oxygen reporting capability of PtP-C343-containing coaxial fibers, cell-seeded fibers were removed at day 7, 10 and 15. PtP-C343-encapsulating fibers were placed in media without PtP-C343 while the PEG-encapsulating fibers were placed in the media with PtP-C343 in solution. As shown, PtP-C343-containing fibers retained oxygen reporting capability after 15 days in the cell culture (Figure 4E and F). While small differences were observed in the phosphorescence decay time constants (τ's) obtained using PtP-C343 in fibers *vs* those of PtP-C343 in solution (red dots vs. blue dots, Figure 4E, $p<0.05$), the calculated pO_2 values using the corresponding calibration curves resulted in near identical pO_2 readings (Figure 4F, $p>0.05$). Similarly, a small difference was observed between the decay time constants using cell-free PtP-C343-containing fibers *vs* PtP-C343 introduced into the surrounding solution (Figure 4G). However, the pO_2 readings were identical when using respective calibration curves for the fibers and solution (Figure 4H).

3.5. PtP-C343-encapsulating Fibers Permit Oxygen Measurements in the Cranial Defect Window Chamber Model in Mice with High Spatial Resolution.

To determine the utility of the PtP-343-encapsulating fibers in oxygen measurements *in vivo*, fiber meshes were implanted into a cranial defect window chamber created in a C57BL/6J mouse, which permits intravital high resolution 3D imaging of bone defect repair[39]. Longitudinal imaging was conducted at days 3, 7, 11, 19, and 32 post-surgery to evaluate healing, while simultaneously probing oxygen tension within the defect via point scans of PtP-C343 phosphorescence (Figure 5A, 1–5). On day 3, phosphorescence decays were obtained within the defect area where the PtP-C343 fiber meshes were located (Figure 5C1). As expected, no phosphorescence could be detected in the areas of the bone surrounding the defect without PtP-C343-containing fibers (Figure 5C2). Using multiple pO_2 measurements within each of the three zones marked in Figure 5A1–5, similar pO_2 readings (35–40 mmHg) were obtained on day 3 (Figure 5D, $p>0.05$). A marked decrease in pO_2 was observed on day 7 post-surgery in all three zones ($p<0.05$), indicating formation of a severely hypoxic environment (*ca.* 11 mmHg), presumably due to the increased oxygen consumption associated with recruitment and influx of cells to the defect. Remarkably, in zones A and B, pO_2 gradually returned to the level of *ca.* 40 mmHg 19 days post-surgery, following revascularization of the defect, as indicated by stereo microscopy imaging of blood vessels during healing (Figure 5B, 1–5). However, pO_2 in the central zone C remained lower than that in the other two regions located closer to the edge of the bone (Figure 5D). After 32 days, the oxygen concentration had reached equilibrium within the entire defect (*ca.* 35 mmHg) with a slightly lower pO_2 observed in the center of the defect. Trends in pO_2 changes during cranial defect repair were similar across multiple animals (Figure S5), suggesting that the observed variations follow a general pattern.

To determine whether the phosphorescence signal from PtP-C343-containing fibers decreased over time, and whether the resultant change in the signal could affect the measurements of the decay times, the ratios of the phosphorescence decay amplitudes to background noise in the three zones were examined. As shown in Figure 5E, the phosphorescence signal amplitude decreased over time, indicating the release and exhaustion of PtP-C343 from the fiber mesh at the implantation sites. However, the signals, at minimum, remained 4-fold higher than background noise even at day 19 post-surgery, which

was sufficient for fitting the data to exponential functions and calculating the phosphorescent decay times (τ). As expected, the decay times were not correlated with signal-to-background ratios. As an example, from the measurements performed in Region A at day 3 and day 19 (Figure 5F), the signal-to-background ratio decreased significantly, but the pO_2 values remained the same. Alternatively, when the signal-to-background ratios were similar, as in days 3 and 7, the lifetimes of phosphorescent decays were different, indicating different pO_2 values. These experiments confirmed that the oxygen measurements *via* 2PLM were independent of the probe concentration and signal intensity. At day 32, the signal-to-noise ratios were markedly reduced leading to large variation in pO_2 values and suggesting a significant decrease in the probe concentration at the site.

To further validate our approach, oxygen-reporting fiber meshes were placed in a 2-mm cranial defect created in a Cdh5CreER^{T2}; Ai9 mouse, in which the blood vessels were marked by red fluorescent protein tdTomato, facilitating separate evaluation of pO_2 in the interstitium and vessels. At day 11 post-surgery, the neovasculature was perfused with PtP-C343, enabling intravascular measurements. Multiple measurements were conducted *via* point scans within vessels and in the nearby interstitial space, where oxygen reporting fibers were located (Figure 6). The average interstitial pO_2 values were binned into groups of 1–10, 10–15, 15–20, and 20–25 μm based on the lateral distances of the nearest vessel. As shown in Figure 6A, the reported pO_2 values were highly spatially resolved in vessels and at the nearby interstitium. Variations of pO_2 within the vessels suggest heterogeneity of oxygen and thus correspond to different vessel types forming in the defect, whether it is arterioles carrying high oxygen or venules with low oxygen. Additionally, with the use of oxygen reporting fibers, measurements can be made to characterize oxygen gradients in the surrounding interstitial space within the healing model. A slightly higher average pO_2 in vessels was noted, suggesting an uneven distribution of oxygen from newly formed vessels to nearby tissue (Figure 6B). No phosphorescence decay signals were observed in interstitium area in defects without insertion of fibers (data not shown), even though PtP-C343 was administered into the circulation for 3 hours, demonstrating the advantage of using oxygen reporting fibers to probe pO_2 in interstitial area where diffusion of the PtP-C343 from the vessels was limited.

Attempts have been made previously to incorporate various oxygen sensitive probes into polymeric fibers for measurements of oxygen distributions in biological environments. For example, Jenkins *et al.* and Yazgan *et al.* utilized porous electrospun fibers that were embedded with a commercially available oxygen reporting molecule PtTFPP.[51, 57] Xue *et al.* encapsulated an oxygen sensitive ruthenium compound in the polyether sulfone (PES) core of PCL sheath coaxial fibers, and oxygen tension changes were inferred from the variations in the phosphorescence intensity.[54–55] Presley *et al.* utilized indirect excitation of phosphorescence for oxygen sensing using upconverting nanoparticles encapsulated within electrospun fibers along with a phosphorescent dye.[53] Bowers *et al.* used a blend of a dual emissive boron poly-lactide-co-glycolic acid (PLAGA) complex and electrospun solid nanofibers for oxygen sensing *in vitro*.[52] The boron complex emits both oxygen-sensitive phosphorescence and oxygen-insensitive fluorescence, thus allowing for ratiometric oxygen quantification. While the ratiometric and intensity-based approaches can be used to quantify oxygen in optically clear solutions, they are not appropriate for quantitative oxygen-sensing

in tissues due to differential absorption and scattering by endogenous chromophores and optical heterogeneities. In contrast, oxygen-reporting fibers used in our work rely exclusively on phosphorescence decay times, which are unaffected neither by optical heterogeneities of the medium nor by the local probe concentration, providing an unbiased quantitative measurement of oxygen. Furthermore, the use of two-photon excitation offers improvements over confocal methods, which were used in the previous studies, through confinement of the excitation volume to the close vicinity of the focus and thus reducing phototoxicity.

In our current approach, the high hydrophilicity of the PtP-C343 probe along with the non-covalent nature of its entrapment within the fibers lead to slow leaching of the probe into the interstitial space. Thus, in addition to their function as a structural foundation for the bone development, the fibers act as a vehicle for delivery of the probe into the healing tissue. In our *in vivo* experiments we observed that a decrease in the signal intensity due to the slow leaching of the probe from the mesh does not affect phosphorescence lifetime measurements during one-month period. Only on day 32 the signal-to-background ratio in the data dropped below the limit where the accuracy in the pO_2 was unacceptable (Region C, Figure 5, D and E). It is important to note that the calibration plots of the probe encapsulated inside the fibers were shown to be dependent on the probe concentration up to 50 μM - the maximal load used in our experiments. This verifies that the calibration plots did not change during the leaching process.

Despite the key role of oxygen in wound healing, few experimental studies utilizing measurements of pO_2 in the newly formed bone have been performed in the past, largely due to the lack of reliable non-invasive methods for real-time measurements of pO_2 in bone healing. As the first attempt at characterizing spatiotemporal changes of oxygen tension in a cranial bone defect healing model, we observed an intriguing pattern of the oxygen tension changes during the first 4 weeks of healing. In three representative zones in the defect, a significant decrease in oxygen at day 7 post-surgery was recorded, followed by gradual restoration of local pO_2 that coincided with the revascularization of the bone defect. A comparison between the pO_2 in the center *vs.* that at the leading edge of the bone defect revealed a difference between these two sites, i.e. a more hypoxic environment in the center of the defect. More in-depth study is needed to determine oxygen distributions within defects and their ultimate impact on bone healing. 2PLM in conjunction with improved two-photon excitable nanosensors, such as the recently developed probe Oxyphor 2P[42] should enable such studies and reveal the relationship between tissue oxygenation and the metabolic activity of bone and vessel forming cells in bone regeneration.

To obtain accurate pO_2 readings, oxygen quenching of the probe was calibrated directly within the PtP-C343-containing fibers (Figure 3). While a small difference at higher pO_2 values was noted between the calibration curves for the probe inside fibers and in solution, our *in vitro* experiments demonstrate that these differences do not affect the final pO_2 readings, especially when using the respective calibration curves (Figure 4E–H). Given the fact that the calibration plots of the probe in the fibers and in solution are quite similar, the phosphorescence decays provided sufficiently accurate average pO_2 values within and around the fibers throughout the most of the oxygen concentration range of interest. It is

noteworthy that the pO_2 values measured in our study are comparable to the previous data obtained in the brain tissue and bone marrow.[27,35]

In order to obtain maximal photon counts, higher laser powers were used in our *in vivo* experiments, which could lead to potential expansion of the excitation volume up to 10–15 μm in Z-direction.[77] However, due to the attenuation by tissue absorption and scattering, the actual 2-photon excitation volume *in vivo* was likely much smaller. In fact, our control measurements, performed in animals containing no fiber meshes upon vascular infusion of PtP-C343, showed strong phosphorescence from the vessels and complete lack of signal when the laser focus was moved into the neighboring extravascular space, suggesting that at the powers used our measurements remained highly spatially localized. Such high confinement of excitation allowed us to evaluate the differences in pO_2 with micron-scale resolution (Figure 6). However, because the diameter of the fibers is below 1–2 micron, when focusing the beam on a fiber, PtP-C343 present inside and outside the mesh could in principle contribute to the overall phosphorescence decay signals. The error introduced by this ambiguity, however, would be minimal, since the calibration curves for the probe inside and outside fibers were found to be very close. Nevertheless, considering that the continued leaching of the probe would eventually lead to the complete loss of the signals from inside the fibers, e.g. more than 30 days post-implantation (Figure 5D), construction of fibers containing non-leaching probes could be advantageous for more localized, but longer-lasting oxygen reporting.

CONCLUSIONS

We have developed an implantable polymeric mesh made of coaxial fibers, capable of reporting oxygen levels during bone defect healing in real time with high spatial resolution. Nanofiber-based delivery of an oxygen sensitive probe allows oxygen measurements during the time when the bone is not yet fully vascularized, while two-photon excitation facilitates high-resolution probing of absolute pO_2 levels *in vivo*. This fibrous matrix could be incorporated into bio-scaffolds to enable oxygen mapping *in vitro* and *in vivo*. The flexible coaxial electrospinning approach could further permit simultaneous delivery of osteogenic and angiogenic factors to the injury sites to facilitate new bone growth, enabling construction of a multifunctional scaffold for oxygen sensing during tissue repair and regeneration. In conjunction with the cranial defect window chamber model, the oxygen-sensing fiber mesh could offer new insights into the role of oxygen in bone repair and ultimately aid in developing novel approaches aimed at manipulating oxygen signaling for improved bone healing.

Supplementary Material

Refer to Web version on PubMed Central for supplementary material.

ACKNOWLEDGEMENTS:

This study is supported by grants NIH R01AR067859, R01DE019902, R21DE02656 to XZ, NIH R21CA208921 and DoD BCRP W81XWH-17-1-0011 to EB, NIH R01EB018464, R24NS092986 and R21EB027397 to SAV and NIH R01AR067859 diversity supplement awarded to KS.

REFERENCES

(1). Lieberman JR; Daluiski A; Einhorn TA The Role of Growth Factors in the Repair of Bone. Biology and Clinical Applications. J Bone Joint Surg Am 2002, 84 (6), 1032–1044. [PubMed: 12063342]

(2). Barnes GL; Kostenuik PJ; Gerstenfeld LC; Einhorn TA Growth Factor Regulation of Fracture Repair. J Bone Miner Res 1999, 14 (11), 1805–1815. [PubMed: 10571679]

(3). Gerstenfeld LC; Cullinane DM; Barnes GL; Graves DT; Einhorn TA Fracture Healing as a Post-Natal Developmental Process: Molecular, Spatial, and Temporal Aspects of Its Regulation. J Cell Biochem 2003, 88 (5), 873–884. [PubMed: 12616527]

(4). Khosla S; Westendorf JJ; Modder UI Concise Review: Insights from Normal Bone Remodeling and Stem Cell-Based Therapies for Bone Repair. Stem Cells 2010, 28 (12), 2124–2128. [PubMed: 20960512]

(5). Carano RA; Filvaroff EH Angiogenesis and Bone Repair. Drug Discov Today 2003, 8 (21), 980–9. [PubMed: 14643161]

(6). Yellowley CE; Genetos DC Hypoxia Signaling in the Skeleton: Implications for Bone Health. Curr Osteoporos Rep 2019, 17 (1), 26–35. [PubMed: 30725321]

(7). Nauta TD; van Hinsbergh VW; Koolwijk P Hypoxic Signaling During Tissue Repair and Regenerative Medicine. International journal of molecular sciences 2014, 15 (11), 19791–19815. [PubMed: 25365172]

(8). Riddle RC; Khatri R; Schipani E; Clemens TL Role of Hypoxia-Inducible Factor-1alpha in Angiogenic-Osteogenic Coupling. J Mol Med (Berl) 2009, 87 (6), 583–590. [PubMed: 19415227]

(9). Wan C; Gilbert SR; Wang Y; Cao X; Shen X; Ramaswamy G; Jacobsen KA; Alaql ZS; Eberhardt AW; Gerstenfeld LC; Einhorn TA; Deng L; Clemens TL Activation of the Hypoxia-Inducible Factor-1alpha Pathway Accelerates Bone Regeneration. Proc Natl Acad Sci U S A 2008, 105 (2), 686–691. [PubMed: 18184809]

(10). Wang Y; Wan C; Deng L; Liu X; Cao X; Gilbert SR; Bouxsein ML; Faugere MC; Guldberg RE; Gerstenfeld LC; Haase VH; Johnson RS; Schipani E; Clemens TL The Hypoxia-Inducible Factor Alpha Pathway Couples Angiogenesis to Osteogenesis During Skeletal Development. J Clin Invest 2007, 117 (6), 1616–1626. [PubMed: 17549257]

(11). Maes C; Carmeliet G; Schipani E Hypoxia-Driven Pathways in Bone Development, Regeneration and Disease. Nature reviews. Rheumatology 2012, 8 (6), 358–366. [PubMed: 22450551]

(12). Schipani E; Ryan HE; Didrickson S; Kobayashi T; Knight M; Johnson RS Hypoxia in Cartilage: Hif-1alpha Is Essential for Chondrocyte Growth Arrest and Survival. Genes Dev 2001, 15 (21), 2865–2876. [PubMed: 11691837]

(13). Ruthenborg RJ; Ban JJ; Wazir A; Takeda N; Kim JW Regulation of Wound Healing and Fibrosis by Hypoxia and Hypoxia-Inducible Factor-1. Molecules and cells 2014, 37 (9), 637–643. [PubMed: 24957212]

(14). Lokmic Z; Musyoka J; Hewitson TD; Darby IA Hypoxia and Hypoxia Signaling in Tissue Repair and Fibrosis. International review of cell and molecular biology 2012, 296, 139–185. [PubMed: 22559939]

(15). Wilson DF Quantifying the Role of Oxygen Pressure in Tissue Function. Am J Physiol Heart Circ Physiol 2008, 294 (1), H11–13. [PubMed: 17993593]

(16). Vanderkooi JM; Maniara G; Green TJ; Wilson DF An Optical Method for Measurement of Dioxygen Concentration Based Upon Quenching of Phosphorescence. J Biol Chem 1987, 262 (12), 5476–5482. [PubMed: 3571219]

(17). Rumsey WL; Vanderkooi JM; Wilson DF Imaging of Phosphorescence: A Novel Method for Measuring Oxygen Distribution in Perfused Tissue. Science 1988, 241 (4873), 1649–1651. [PubMed: 3420417]

(18). Papkovsky DB; Dmitriev RI Biological Detection by Optical Oxygen Sensing. Chemical Society reviews 2013, 42 (22), 8700–8732. [PubMed: 23775387]

(19). Quaranta M; Borisov SM; Klimant I Indicators for Optical Oxygen Sensors. Bioanalytical reviews 2012, 4 (2–4), 115–157. [PubMed: 23227132]

(20). Wang XD; Wolfbeis OS Optical Methods for Sensing and Imaging Oxygen: Materials, Spectroscopies and Applications. Chemical Society reviews 2014, 43 (10), 3666–3761. [PubMed: 24638858]

(21). Roussakis E; Li Z; Nichols AJ; Evans CL Oxygen-Sensing Methods in Biomedicine from the Macroscale to the Microscale. Angew Chem Int Ed Engl 2015, 54 (29), 8340–8362. [PubMed: 26084034]

(22). Yoshihara T; Hirakawa Y; Hosaka M; Nangaku M; Tobita S Oxygen Imaging of Living Cells and Tissues Using Luminescent Molecular Probes. J Photoch Photobio C 2017, 30, 71–95.

(23). Lebedev AY; Cheprakov AV; Sakadzic S; Boas DA; Wilson DF; Vinogradov SA Dendritic Phosphorescent Probes for Oxygen Imaging in Biological Systems. ACS applied materials & interfaces 2009, 1 (6), 1292–1304. [PubMed: 20072726]

(24). Esipova TV; Karagodov A; Miller J; Wilson DF; Busch TM; Vinogradov SA Two New "Protected" Oxyphors for Biological Oximetry: Properties and Application in Tumor Imaging. Analytical chemistry 2011, 83 (22), 8756–8765. [PubMed: 21961699]

(25). Finikova OS; Lebedev AY; Aprelev A; Troxler T; Gao F; Garnacho C; Muro S; Hochstrasser RM; Vinogradov SA Oxygen Microscopy by Two-Photon-Excited Phosphorescence. Chemphyschem : a European journal of chemical physics and physical chemistry 2008, 9 (12), 1673–1679. [PubMed: 18663708]

(26). Zipfel WR; Williams RM; Webb WW Nonlinear Magic: Multiphoton Microscopy in the Biosciences. Nat Biotechnol 2003, 21 (11), 1369–1377. [PubMed: 14595365]

(27). Sakadzic S; Roussakis E; Yaseen MA; Mandeville ET; Srinivasan VJ; Arai K; Ruvinskaya S; Devor A; Lo EH; Vinogradov SA; Boas DA Two-Photon High-Resolution Measurement of Partial Pressure of Oxygen in Cerebral Vasculature and Tissue. Nat Methods 2010, 7 (9), 755–759. [PubMed: 20693997]

(28). Lecoq J; Parpaleix A; Roussakis E; Ducros M; Goulam Houssen Y; Vinogradov SA; Charpak S Simultaneous Two-Photon Imaging of Oxygen and Blood Flow in Deep Cerebral Vessels. Nat Med 2011, 17 (7), 893–898. [PubMed: 21642977]

(29). Devor A; Sakadzic S; Saisan PA; Yaseen MA; Roussakis E; Srinivasan VJ; Vinogradov SA; Rosen BR; Buxton RB; Dale AM; Boas DA "Overshoot" of O(2) Is Required to Maintain Baseline Tissue Oxygenation at Locations Distal to Blood Vessels. J Neurosci 2011, 31 (38), 13676–13681. [PubMed: 21940458]

(30). Parpaleix A; Goulam Houssen Y; Charpak S Imaging Local Neuronal Activity by Monitoring Po(2) Transients in Capillaries. Nat Med 2013, 19 (2), 241–246. [PubMed: 23314058]

(31). Lyons DG; Parpaleix A; Roche M; Charpak S Mapping Oxygen Concentration in the Awake Mouse Brain. eLife 2016, 5.

(32). Kazmi SM; Salvaggio AJ; Estrada AD; Hemati MA; Shaydyuk NK; Roussakis E; Jones TA; Vinogradov SA; Dunn AK Three-Dimensional Mapping of Oxygen Tension in Cortical Arterioles before and after Occlusion. Biomedical optics express 2013, 4 (7), 1061–1073. [PubMed: 23847732]

(33). Sakadzic S; Mandeville ET; Gagnon L; Musacchia JJ; Yaseen MA; Yucel MA; Lefebvre J; Lesage F; Dale AM; Eikermann-Haerter K; Ayata C; Srinivasan VJ; Lo EH; Devor A; Boas DA Large Arteriolar Component of Oxygen Delivery Implies a Safe Margin of Oxygen Supply to Cerebral Tissue. Nature communications 2014, 5, 5734.

(34). Kisler K; Nelson AR; Rege SV; Ramanathan A; Wang Y; Ahuja A; Lazic D; Tsai PS; Zhao Z; Zhou Y; Boas DA; Sakadzic S; Zlokovic BV Pericyte Degeneration Leads to Neurovascular Uncoupling and Limits Oxygen Supply to Brain. Nature neuroscience 2017, 20 (3), 406–416. [PubMed: 28135240]

(35). Spencer JA; Ferraro F; Roussakis E; Klein A; Wu J; Runnels JM; Zaher W; Mortensen LJ; Alt C; Turcotte R; Yusuf R; Cote D; Vinogradov SA; Scadden DT; Lin CP Direct Measurement of Local Oxygen Concentration in the Bone Marrow of Live Animals. Nature 2014, 508 (7495), 269–273. [PubMed: 24590072]

(36). Roussakis E; Ortines RV; Pinsker BL; Mooers CT; Evans CL; Miller LS; Calderon-Colon X Theranostic Biocomposite Scaffold Membrane. Biomaterials 2019, 212, 17–27. [PubMed: 31100480]

(37). Okkelman IA; Foley T; Papkovsky DB; Dmitriev RI Live Cell Imaging of Mouse Intestinal Organoids Reveals Heterogeneity in Their Oxygenation. Biomaterials 2017, 146, 86–96. [PubMed: 28898760]

(38). Rytelewski M; Haryutyunan K; Nwajei F; Shanmugasundaram M; Wspanialy P; Zal MA; Chen CH; El Khatib M; Plunkett S; Vinogradov SA; Konopleva M; Zal T Merger of Dynamic Two-Photon and Phosphorescence Lifetime Microscopy Reveals Dependence of Lymphocyte Motility on Oxygen in Solid and Hematological Tumors. Journal for immunotherapy of cancer 2019, 7 (1), 78. [PubMed: 30885258]

(39). Huang C; Ness VP; Yang X; Chen H; Luo J; Brown EB; Zhang X Spatiotemporal Analyses of Osteogenesis and Angiogenesis Via Intravital Imaging in Cranial Bone Defect Repair. J Bone Miner Res 2015, 30 (7), 1217–1230. [PubMed: 25640220]

(40). Brinas RP; Troxler T; Hochstrasser RM; Vinogradov SA Phosphorescent Oxygen Sensor with Dendritic Protection and Two-Photon Absorbing Antenna. J Am Chem Soc 2005, 127 (33), 11851–11862. [PubMed: 16104764]

(41). Roussakis E; Spencer JA; Lin CP; Vinogradov SA Two-Photon Antenna-Core Oxygen Probe with Enhanced Performance. Analytical chemistry 2014, 86 (12), 5937–5945. [PubMed: 24848643]

(42). Esipova TV; Barrett MJP; Erlebach E; Masunov AE; Weber B; Vinogradov SA Oxyphor 2p: A High-Performance Probe for Deep-Tissue Longitudinal Oxygen Imaging. Cell Metab 2019, 29 (3), 736–744. [PubMed: 30686745]

(43). Subramony SD; Dargis BR; Castillo M; Azeloglu EU; Tracey MS; Su A; Lu HH The Guidance of Stem Cell Differentiation by Substrate Alignment and Mechanical Stimulation. Biomaterials 2013, 34 (8), 1942–1953. [PubMed: 23245926]

(44). Dahlin RL; Kasper FK; Mikos AG Polymeric Nanofibers in Tissue Engineering. Tissue Eng Part B Rev 2011, 17 (5), 349–364. [PubMed: 21699434]

(45). Liu W; Thomopoulos S; Xia Y Electrospun Nanofibers for Regenerative Medicine. Advanced healthcare materials 2012, 1 (1), 10–25. [PubMed: 23184683]

(46). Baker BM; Handorf AM; Ionescu LC; Li WJ; Mauck RL New Directions in Nanofibrous Scaffolds for Soft Tissue Engineering and Regeneration. Expert review of medical devices 2009, 6 (5), 515–532. [PubMed: 19751124]

(47). Sill TJ; von Recum HA Electrospinning: Applications in Drug Delivery and Tissue Engineering. Biomaterials 2008, 29 (13), 1989–2006. [PubMed: 18281090]

(48). Pham QP; Sharma U; Mikos AG Electrospinning of Polymeric Nanofibers for Tissue Engineering Applications: A Review. Tissue Eng 2006, 12 (5), 1197–1211. [PubMed: 16771634]

(49). McCann JT; Marquez M; Xia Y Melt Coaxial Electrospinning: A Versatile Method for the Encapsulation of Solid Materials and Fabrication of Phase Change Nanofibers. Nano Lett 2006, 6 (12), 2868–2872. [PubMed: 17163721]

(50). Sultanova Z; Kaleli G; Kabay G; Mutlu M Controlled Release of a Hydrophilic Drug from Coaxially Electrospun Polycaprolactone Nanofibers. Int J Pharm 2016, 505 (1–2), 133–138. [PubMed: 27012983]

(51). Yazgan G; Dmitriev RI; Tyagi V; Jenkins J; Rotaru GM; Rottmar M; Rossi RM; Toncelli C; Papkovsky DB; Maniura-Weber K; Fortunato G Steering Surface Topographies of Electrospun Fibers: Understanding the Mechanisms. Sci Rep 2017, 7 (1), 158. [PubMed: 28279011]

(52). Bowers DT; Tanes ML; Das A; Lin Y; Keane NA; Neal RA; Ogle ME; Brayman KL; Fraser CL; Botchwey EA Spatiotemporal Oxygen Sensing Using Dual Emissive Boron Dye-Polylactide Nanofibers. ACS nano 2014, 8 (12), 12080–12091. [PubMed: 25426706]

(53). Presley K; Hwang J; Cheong S; Tilley R; Collins J; Viapiano M; Lannutti J Nanoscale Upconversion for Oxygen Sensing. Mater Sci Eng C Mater Biol Appl 2017, 70 (Pt 1), 76–84. [PubMed: 27770952]

(54). Xue R; Behera P; Viapiano MS; Lannutti JJ Rapid Response Oxygen-Sensing Nanofibers. Mater Sci Eng C Mater Biol Appl 2013, 33 (6), 3450–3457. [PubMed: 23706233]

(55). Xue R; Ge C; Richardson K; Palmer A; Viapiano M; Lannutti JJ Microscale Sensing of Oxygen Via Encapsulated Porphyrin Nanofibers: Effect of Indicator and Polymer “Core” Permeability. ACS applied materials & interfaces 2015, 7 (16), 8606–8614. [PubMed: 25850567]

(56). Okkelman IA; Dolgova AA; Banerjee S; Kerry JP; Volynskii A; Arzhakova OV; Papkovsky DB Phosphorescent Oxygen and Mechanosensitive Nanostructured Materials Based on Hard Elastic Polypropylene Films. ACS applied materials & interfaces 2017, 9 (15), 13587–13592. [PubMed: 28367617]

(57). Jenkins J; Dmitriev RI; Morten K; McDermott KW; Papkovsky DB Oxygen-Sensing Scaffolds for 3-Dimensional Cell and Tissue Culture. Acta Biomater 2015, 16, 126–135. [PubMed: 25653216]

(58). Borisov SM; Pommer R; Svec J; Peters S; Novakova V; Klimant I New Red-Emitting Schiff Base Chelates: Promising Dyes for Sensing and Imaging of Temperature and Oxygen Via Phosphorescence Decay Time. Journal of materials chemistry. C 2018, 6 (33), 8999–9009. [PubMed: 30713692]

(59). Dmitriev RI; Borisov SM; Dussmann H; Sun S; Muller BJ; Prehn J; Baklaushev VP; Klimant I; Papkovsky DB Versatile Conjugated Polymer Nanoparticles for High-Resolution O2 Imaging in Cells and 3d Tissue Models. ACS nano 2015, 9 (5), 5275–5288. [PubMed: 25858428]

(60). Lebedev AY; Troxler T; Vinogradov SA Design of Metalloporphyrin-Based Dendritic Nanoprobes for Two-Photon Microscopy of Oxygen. J Porphyr Phthalocyanines 2008, 12 (12), 1261–1269. [PubMed: 19763243]

(61). Yew CHT; Azari P; Choi JR; Muhamad F; Pingguan-Murphy B Electrospun Polycaprolactone Nanofibers as a Reaction Membrane for Lateral Flow Assay. Polymers 2018, 10 (12), 1387.

(62). Stalder AF; Melchior T; Muller M; Sage D; Blu T; Unser M Low-Bond Axisymmetric Drop Shape Analysis for Surface Tension and Contact Angle Measurements of Sessile Drops. Colloid Surface A 2010, 364 (1–3), 72–81.

(63). Lyu S; Huang C; Yang H; Zhang X Electrospun Fibers as a Scaffolding Platform for Bone Tissue Repair. J Orthop Res 2013, 31 (9), 1382–9. [PubMed: 23580466]

(64). Wang T; Zhai Y; Nuzzo M; Yang X; Yang Y; Zhang X Layer-by-Layer Nanofiber-Enabled Engineering of Biomimetic Periosteum for Bone Repair and Reconstruction. Biomaterials 2018, 182, 279–288. [PubMed: 30142527]

(65). Cheng G; Yin C; Tu H; Jiang S; Wang Q; Zhou X; Xing X; Xie C; Shi X; Du Y; Deng H; Li Z Controlled Co-Delivery of Growth Factors through Layer-by-Layer Assembly of Core-Shell Nanofibers for Improving Bone Regeneration. ACS nano 2019, 13 (6), 6372–6382. [PubMed: 31184474]

(66). Gong M; Huang C; Huang Y; Li G; Chi C; Ye J; Xie W; Shi R; Zhang L Core-Sheath Micro/Nano Fiber Membrane with Antibacterial and Osteogenic Dual Functions as Biomimetic Artificial Periosteum for Bone Regeneration Applications. Nanomedicine : nanotechnology, biology, and medicine 2019, 17, 124–136.

(67). Yao Q; Cosme JG; Xu T; Miszuk JM; Picciani PH; Fong H; Sun H Three Dimensional Electrospun Pcl/Pla Blend Nanofibrous Scaffolds with Significantly Improved Stem Cells Osteogenic Differentiation and Cranial Bone Formation. Biomaterials 2017, 115, 115–127. [PubMed: 27886552]

(68). Woodruff MA; Hutmacher DW The Return of a Forgotten Polymer-Polycaprolactone in the 21st Century. Prog Polym Sci 2010, 35 (10), 1217–1256.

(69). Jiang H; Hu Y; Li Y; Zhao P; Zhu K; Chen W A Facile Technique to Prepare Biodegradable Coaxial Electrospun Nanofibers for Controlled Release of Bioactive Agents. Journal of controlled release : official journal of the Controlled Release Society 2005, 108 (2–3), 237–243.

(70). Nasehi F; Karshenas M; Nadri S; Barati G; Salim A Core-Shell Fibrous Scaffold as a Vehicle for Sustained Release of Retinal Pigmented Epithelium-Derived Factor (Pedf) for Photoreceptor Differentiation of Conjunctiva Mesenchymal Stem Cells. J Biomed Mater Res A 2017, 105 (12), 3514–3519. [PubMed: 28795779]

(71). Saraf A; Lozier G; Haesslein A; Kasper FK; Raphael RM; Baggett LS; Mikos AG Fabrication of Nonwoven Coaxial Fiber Meshes by Electrospinning. Tissue Eng Part C Methods 2009, 15 (3), 333–344. [PubMed: 19196125]

(72). Yoon J; Yang HS; Lee BS; Yu WR Recent Progress in Coaxial Electrospinning: New Parameters, Various Structures, and Wide Applications. Adv Mater 2018, 30 (42), e1704765. [PubMed: 30152180]

(73). Zhang YZ; Wang X; Feng Y; Li J; Lim CT; Ramakrishna S Coaxial Electrospinning of (Fluorescein Isothiocyanate-Conjugated Bovine Serum Albumin)-Encapsulated Poly(Epsilon-Caprolactone) Nanofibers for Sustained Release. Biomacromolecules 2006, 7 (4), 1049–1057. [PubMed: 16602720]

(74). Lu Y; Huang J; Yu G; Cardenas R; Wei S; Wujcik EK; Guo Z Coaxial Electrospun Fibers: Applications in Drug Delivery and Tissue Engineering. Wiley interdisciplinary reviews. Nanomedicine and nanobiotechnology 2016, 8 (5), 654–677. [PubMed: 26848106]

(75). Drexler JW; Powell HM Regulation of Electrospun Scaffold Stiffness Via Coaxial Core Diameter. Acta Biomaterialia 2011, 7 (3), 1133–1139. [PubMed: 20977951]

(76). Hou LJ; Zhang X; Mikael PE; Lin L; Dong WJ; Zhen YY; Simmons TJ; Zhang FM; Linhardt RJ Biodegradable and Bioactive Pcl-Pgs Core-Shell Fibers for Tissue Engineering. Acs Omega 2017, 2 (10), 6321–6328. [PubMed: 30023516]

(77). Sinks LE; Robbins GP; Roussakis E; Troxler T; Hammer DA; Vinogradov SA Two-Photon Microscopy of Oxygen: Polymersomes as Probe Carrier Vehicles. J Phys Chem B 2010, 114 (45), 14373–14382. [PubMed: 20462225]

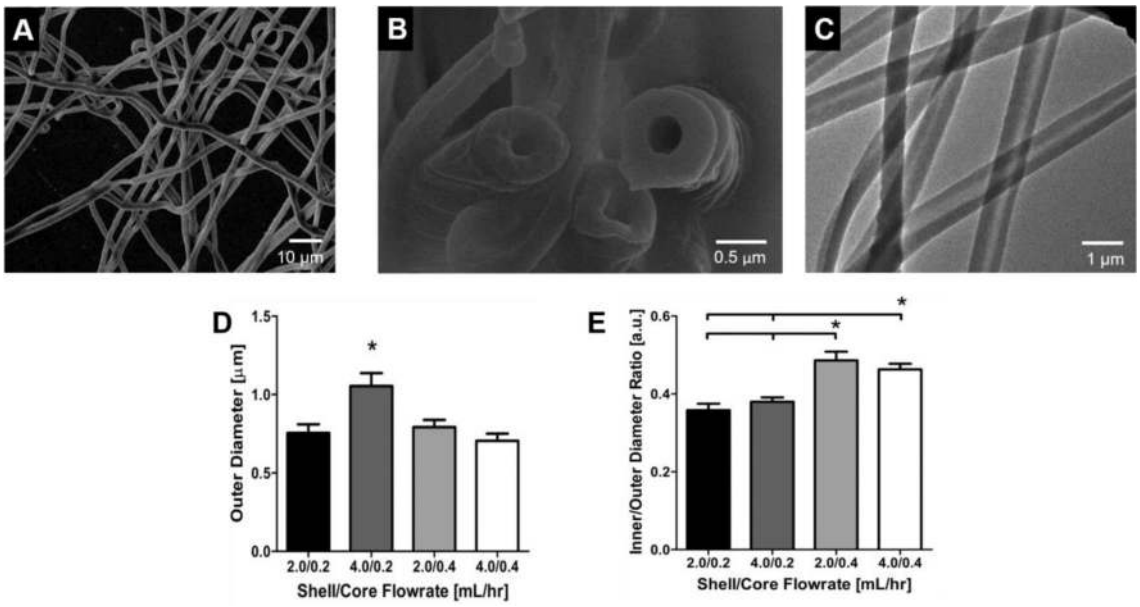

Figure 1. Characterization of the coaxial fibers via SEM and TEM.

Representative SEM images of coaxial electrospun fibers (A) and their cross sections upon freeze-fracturing (B). TEM image shows high percentage of fibers with hollow structure (C). Changes in sheath/core flow rates yield coaxial fibers with varying outer diameters (D) (n=45 per group) and inner-to-outer diameter ratios (E) (n=20 per group).

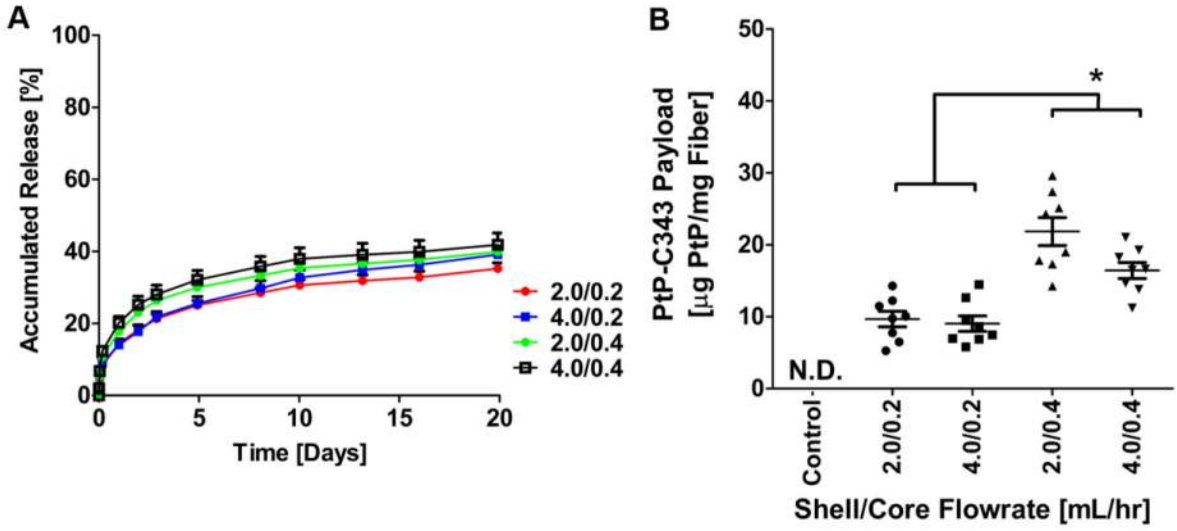

Figure 2. PtP-C343 release from the coaxial fibers.

The accumulated release of PtP-C343 from coaxial fibers fabricated at the four different combinations of flow rates at 37 °C (A). n=4 fiber meshes per group. The amount of PtP-C343 loading in fiber meshes obtained at different combinations of flow rates (B).

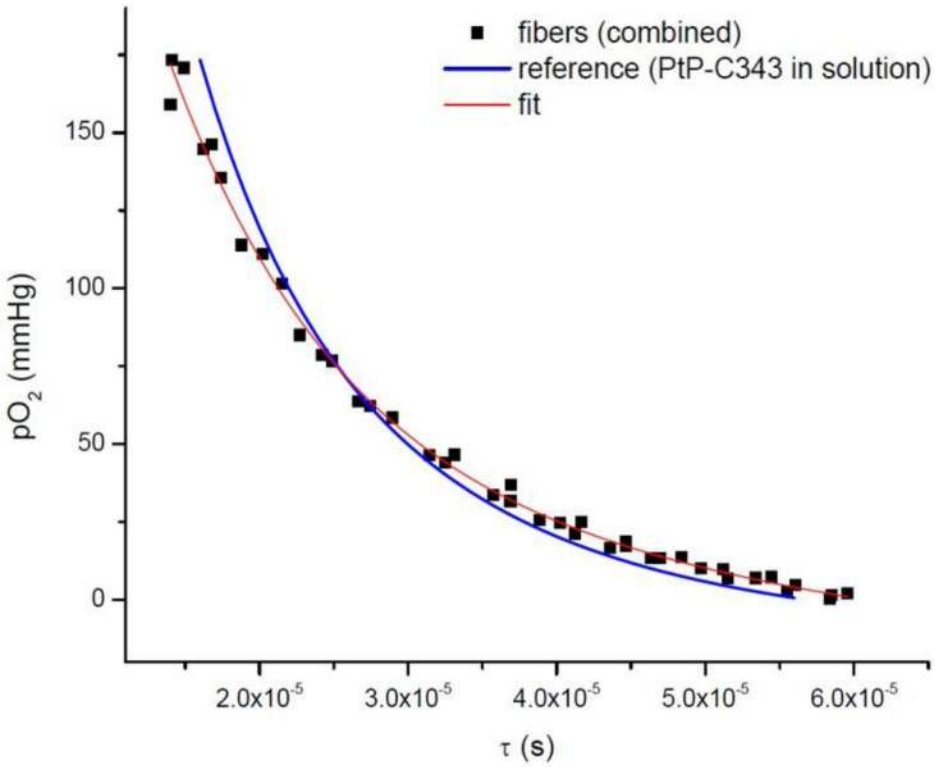

Figure 3. Calibrations of PtP-C343 inside fibers (black squares) and in solution (blue line).
Data from PtP-C343 inside fibers represent measurements in multiple meshes (n=5).

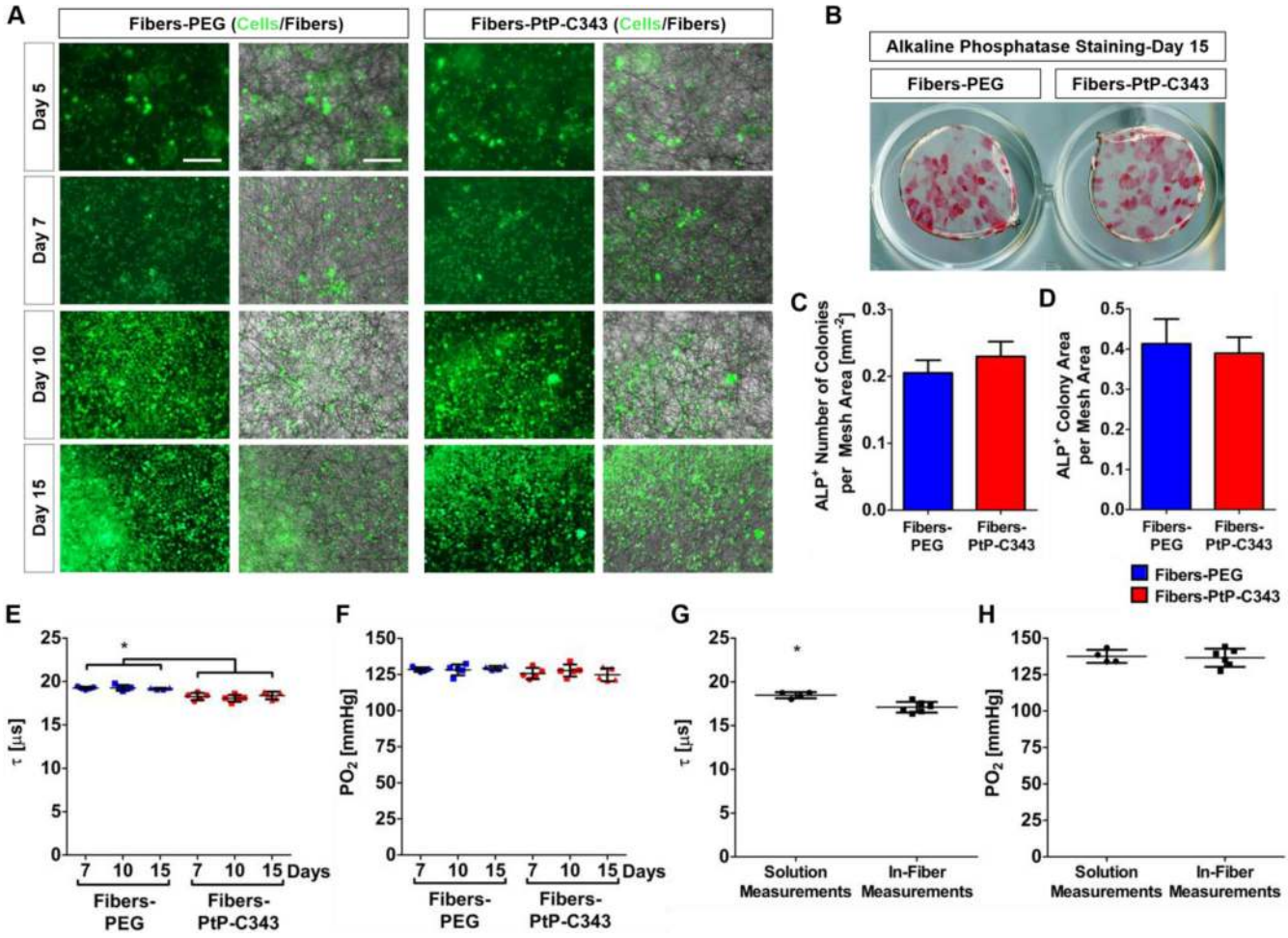

Figure 4. Comparison of coaxial fibers with or without PtP-C343 in BMSC culture.

GFP^+ BMSCs seeded on coaxial fibers with or without PtP-C343 at days 5, 7, 10 and 15 (A). Scale bar = 200 μm. Representative images of ALP^+ BMSC colonies on fibers with or without PtP-C343 at day 15 (B). Quantitative measurements of the number (C) and size (D) of ALP+ colonies. The decay time constant (τ) (E) and pO_2 (F) obtained from PtP-C343 in solution (blue dots) or PtP-C343 in fiber (red dots) via 2PLM at days 7, 10 and 15 post-seeding. The respective decay time constant (G) and pO_2 (H) in cell free coaxial fibers with or without PtP-C343. The pO_2 values were calculated using respective calibration curves.

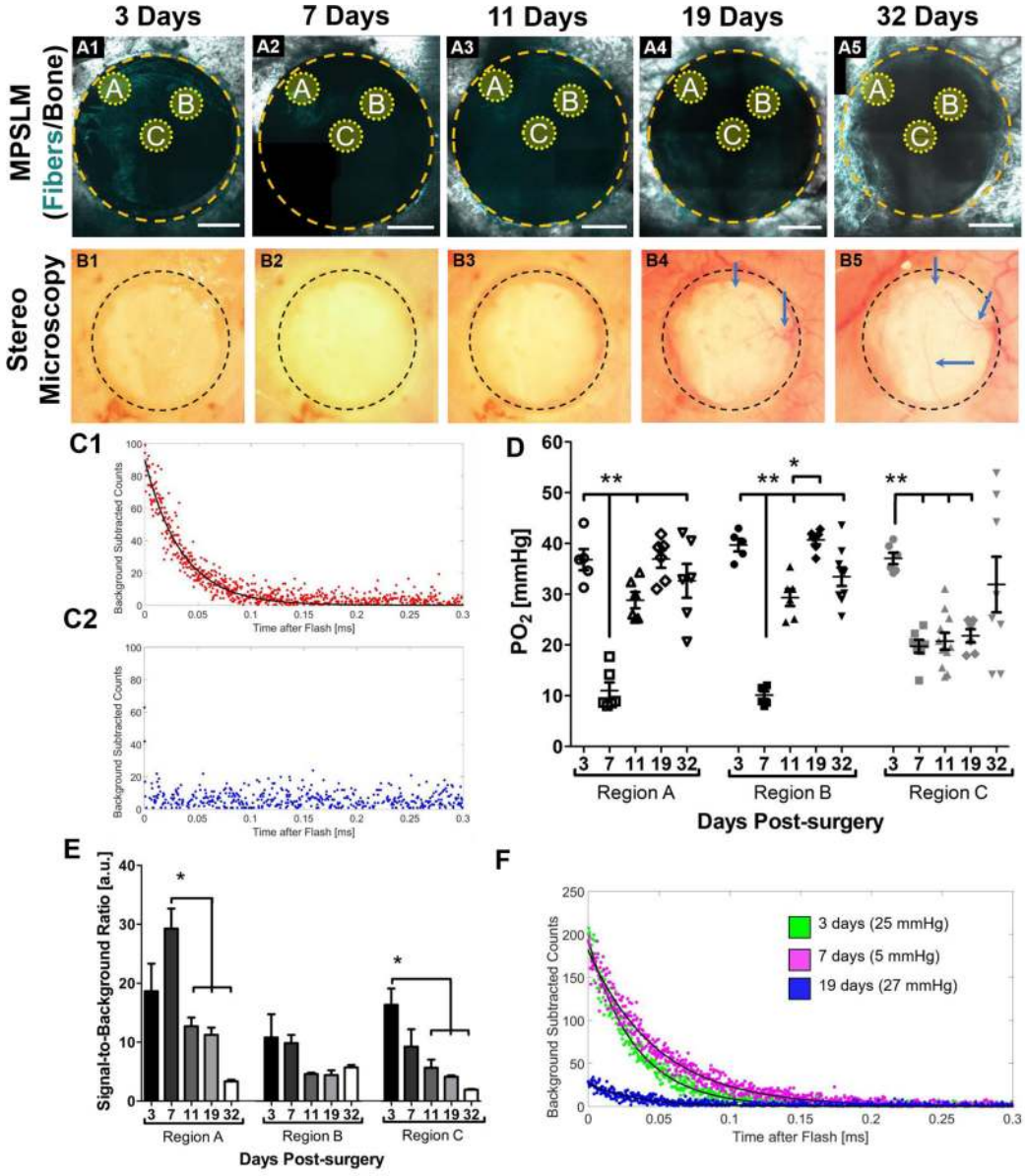

Figure 5. ***In vivo*** **pO_2 reported by PtP-C343-loaded coaxial fibers in cranial defect.**

Longitudinal two-photon images of the cranial window (A1–5) and the corresponding regular light microscopy images of the defect during bone healing (B1–5) (scale bar = 0.25 mm). Fiber shown as cyan, and bone/SHG shown as white. Dashed orange line indicates the initial defect area. Arrows in B4 and B5 indicate the development of visible vessels within defect. Oxygen measurements via 2PLM were performed longitudinally in regions A-C as marked in A1–5. Point 2PLM scan within the defect zone resulted in phosphorescent decays (C1). No phosphorescent decays were observed when exciting the bone (C2). Longitudinal pO_2 measurements within the marked zones (D) (**, $p<0.01$). The phosphorescent decay curve signal-to-background ratios at each zone (E). For comparison, decay curves at days 3, 7 and 19 within region A are shown (F).

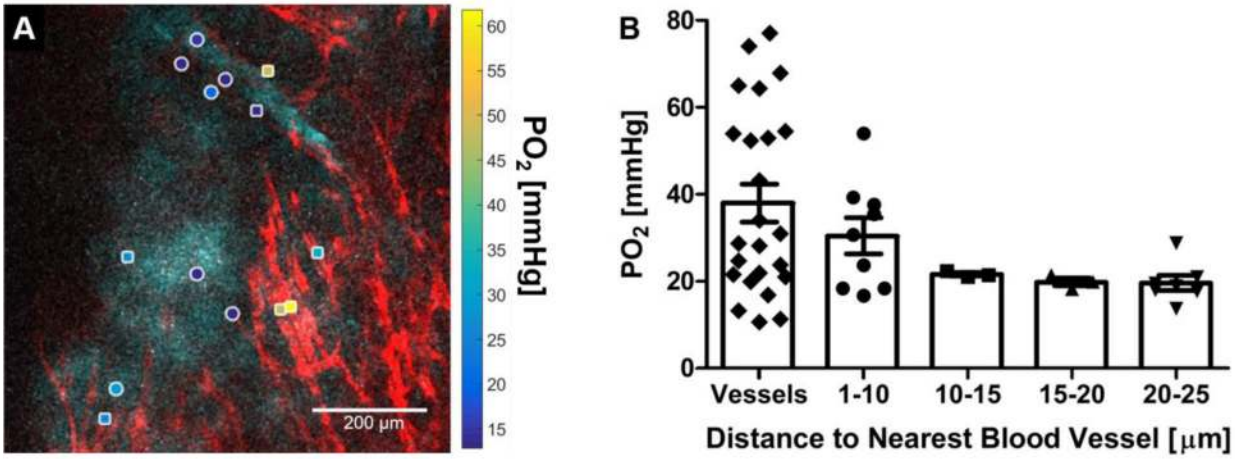

Figure 6.

In vivo pO_2 measurements in vasculature and tissue interstitium *via* PtP-C343-loaded coaxial fibers. The PtP-C343-loaded coaxial fibers were inserted into a 2-mm defect created in the cranial window of Cdh5CreER^{T2};Ai9 mouse model with blood vessels marked with red fluorescent protein tdTomato. Imaging was performed on day 11 post surgery. Reconstructed images of the defect show PtP-C343-loaded coaxial fibers (cyan) and blood vessels (red). An overlay of points where pO_2 measurements were made with a corresponding mean pO_2 is shown *via* color bar. The squares indicate measurements within vessels and circles in the interstitium (A). All pO_2 reported in vessels and interstitium were plotted based on their lateral distance to the nearest blood vessel (B).